ELSEVIER

Computational Materials Science 12 (1998) 105–123

COMPUTATIONAL MATERIALS SCIENCE

Finite element simulations of cold deformation at the mesoscale

G.B. Sarma *, B. Radhakrishnan, T. Zacharia

Computational Materials Science Group, Oak Ridge National Laboratory, P.O. Box 2008 MS 6140, Oak Ridge, TN 37831-6140, USA

Received 6 April 1998; accepted 1 July 1998

Abstract

The deformation of polycrystalline aggregates is modeled using the finite element method. Explicit discretization at the single crystal level is employed to study the inhomogeneous deformations of individual crystals. Plastic deformation by crystallographic slip is treated using a constitutive model based on crystal plasticity. The formulation is used to predict the non-uniform nature of strain hardening and texture evolution in the crystals subjected to plane strain compression. The capability of the simulations to capture the inhomogeneous deformation of individual grains during plastic deformation of polycrystals is demonstrated. The hardness and orientation values of elements from the same grain evolve to different final values due to local inhomogeneities and interactions with neighbors. The simulations provide a means to obtain quantitative information on the inhomogeneous distributions of stored energy and orientations among the different crystals comprising the microstructure. © 1998 Published by Elsevier Science B.V. All rights reserved.

Keywords: Finite element method; Mesoscale modeling; Texture development; Crystal plasticity; Inhomogeneous deformations

1. Introduction

In metals deformed under cold working conditions, the increase in dislocation density causes a portion of the work done to be retained as stored energy of deformation. The stored energy is released during subsequent annealing by the processes of recovery and recrystallization [1]. During recovery, the dislocations rearrange themselves into configurations of lower energy and form low angle boundaries. During recrystallization, strain-free nuclei with high angle grain boundaries form and grow, leading to further decrease in stored energy. These phenomena are of particular significance in metals and alloys subjected to thermo-mechanical processing, since the resulting microstructure is determined by the processing variables. Predicting the microstructure resulting from processing has been the subject of much research, but the models used for this purpose do not incorporate all the parameters necessary for a complete quantitative description. Modeling the kinetics and the evolution of the grain structure and texture during recrystallization requires knowledge of the non-uniform distributions of stored energy and orientations in the cold worked material.

* Corresponding author. Tel.: +1 423 574 5147; fax: +1 423 574 7463; e-mail: saramag@ornl.gov

0927-0256/98/$ – see front matter © 1998 Published by Elsevier Science B.V. All rights reserved.
PII: S 0 9 2 7 - 0 2 5 6 (9 8) 0 0 0 3 6 - 6

In this article, a novel finite element formulation is presented for modeling the microstructural evolution during cold deformation of metals, that generates quantitative information on the stored energy and orientation distributions in the deformed microstructure. By means of explicit discretization of grains at the microstructural level, the finite element analysis permits modeling the inhomogeneous deformation of the grains to predict changes in grain shape, orientation and the non-uniform stored energy distribution.

In recent years, there have been several studies at the microstructural length scales, where the deformation of polycrystals has been simulated using the finite element method [2–7]. These simulations proceed by discretizing an aggregate of grains and applying boundary conditions corresponding to a homogeneous macroscopic deformation to the mesh. The inhomogeneous deformation of the aggregate is influenced by the interactions at grain boundaries, in addition to the differences in properties among individual grains. By placing numerous elements in a single grain, it is possible to capture the non-uniform deformation within a grain. By making use of a crystal plasticity model for the constitutive response, these studies have been able to model the evolution of grain orientation, and hence the development of crystallographic texture.

Harren and Asaro [2] studied a model two-dimensional polycrystal made up of rate dependent planar crystals. Deformations of 27 crystals discretized with 40×56 quadrilateral elements in tension, compression and simple shear were simulated and compared with predictions using a Taylor-type [8] model. The results of their simulations showed the formation of macroscopic shear bands and sub-grains. Localized shearing and non-uniform deformations occurred due to the nature of deformation by crystallographic slip, and the influence of grain interactions.

Becker [4] conducted a similar study using an idealized two-dimensional geometric model deformed in plane strain compression. However, the material behavior in each element was determined assuming an FCC crystal structure using a rate dependent constitutive model. A mesh containing 60×24 quadrilateral elements was employed. The results of the analyses reveal complex deformation patterns arising from grain interactions, with both the overall texture and the spread of orientations within a grain being influenced not only by the orientations of the neighboring grains, but also by the constraints provided by grains located several grains away.

Bronkhorst et al. [5] simulated the deformation of FCC polycrystals in a manner similar to Becker [4]. Tension and compression were simulated using cubic mesh with seven brick elements along each side, while a planar mesh of 20×20 elements was used for plane strain compression and simple shear. The predicted textures using the finite element approach matched experimental data better than a Taylor-like model. Anand and Kalidindi [6] used the same approach to examine the effect of crystallographic texture on the formation of shear bands during plane strain compression.

Becker and Panchanadeeswaran [7] conducted simulations of a planar section of polycrystalline aluminum deformed in channel-die compression. Their results showed the influence of grain interaction on local deformation and texture evolution.

While the above simulations were restricted to planar microstructures and relatively coarse discretizations, with the help of parallel computing methods, some recent efforts have been able to treat fairly large three-dimensional meshes [9–11]. Beaudoin et al. [9] employed a hybrid finite element formulation to study the deformation of a polycrystal under plane strain compression. The simulation used a $16 \times 16 \times 16$ mesh of eight-noded brick elements with one FCC crystal per element. The resulting texture evolution was compared with other models and experimental data. It was shown that the finite element calculation leads to better match with experiment, for both the intensities and the locations of texture components. Based on the same formulation, Sarma and Dawson [10] simulated deformations of FCC polycrystals to examine the distribution of deformation among the individual crystals. The results of the study showed that interactions among crystals play a dominant role in the determining the spread of the applied deformation among them.

Recently, Beaudoin et al. [11] examined the origin of possible nucleation sites for recrystallization by simulating plane strain compression of model polycrystals. These simulations employed fairly large three-dimensional meshes to study the heterogeneous deformation of the individual crystals, and found that some of the elements rotated to near cube orientations after heavy reductions.

The objectives of the current effort are two-fold. The first is to apply the finite element deformation model to a realistic microstructure. Previous efforts using this approach have been restricted to 2-D microstructures or 3-D models with special configurations. This work constitutes the first attempt at simulating a fully three-dimensional microstructure with discretization of individual grains. The second objective of this work is to combine the deformation model with a recovery and recrystallization model. Previous work at the microstructural length scale has focused on one or the other aspect of processing. In this work, the deformation model is used to provide more realistic initial data to the recrystallization model. The coupling of results from this study to model recovery and recrystallization phenomena is described elsewhere [12].

In the following section, the finite element formulation and the constitutive assumptions used in the present study are described. In Section 3, the application of the method to simulate cold deformation to different strains is discussed, and some results on the stored energy and orientation distributions are presented. This is followed by some closing remarks in Section 4.

2. Finite element formulation

The details of the finite element formulation used for simulating the cold deformation are available elsewhere [9], and only the main features are recalled here. It is assumed that elastic deformations are negligibly small, and that deformation occurs by slip dominated plastic flow of the material. Due to the limited modes of deformation available through slip, the crystals must rotate to accommodate arbitrary deformations. The preferred reorientation of crystals leads to texture development, and is modeled using a constitutive law based on crystal plasticity.

A viscoplastic constitutive law relates the rate of shearing $\dot{\gamma}^{(\alpha)}$ to the resolved shear stress $\tau^{(\alpha)}$ on each slip system (α) [13–16]:

$$\dot{\gamma}^{(\alpha)} = \dot{\gamma}_0 \left| \frac{\tau^{(\alpha)}}{\hat{\tau}} \right|^{1/m} \operatorname{sign}(\tau^{(\alpha)}), \tag{1}$$

where m is the rate sensitivity parameter, and $\dot{\gamma}_0$ is a reference rate of shearing. $\hat{\tau}$ is a hardness parameter which represents resistance to plastic deformation due to interactions among dislocations. The resolved shear stress is the component of the traction along the slip direction, and is obtained from the crystal deviatoric Cauchy stress $\boldsymbol{\sigma}'_c$ using the Schmid tensor (dyadic product of the slip direction $\mathbf{s}^{(\alpha)}$ and the slip plane normal $\mathbf{n}^{(\alpha)}$ vectors),

$$\tau^{(\alpha)} = \boldsymbol{\sigma}'_c \mathbf{n}^{(\alpha)} \cdot \mathbf{s}^{(\alpha)} = \boldsymbol{\sigma}'_c \cdot \mathbf{T}^{(\alpha)} = \boldsymbol{\sigma}'_c \cdot \mathbf{P}^{(\alpha)}. \tag{2}$$

In the above expression, $\mathbf{P}^{(\alpha)}$ is the symmetric portion of the Schmid tensor $\mathbf{T}^{(\alpha)}$, and is used to express the crystal rate of deformation $\mathbf{D}_c$ as a linear combination of the slip system shearing rates,

$$\mathbf{D}_c = \sum_{\alpha} \dot{\gamma}^{(\alpha)} \mathbf{P}^{(\alpha)}. \tag{3}$$

The crystal rate of deformation is the symmetric part of the crystal velocity gradient, and prescribes the rate of shearing of slip planes. The skew-symmetric part of the crystal velocity gradient $\mathbf{W}_c$ controls the rotation of the crystal, and contains contributions from both the spin associated with the plastic flow, and the rigid rotation $\mathbf{R}^*$ of the crystal lattice necessary to maintain compatibility with neighboring crystals,

$$\mathbf{W}_c = \dot{\mathbf{R}}^* \mathbf{R}^{*^T} + \sum_\alpha \dot{\gamma}^{(\alpha)} \mathbf{Q}^{(\alpha)}, \tag{4}$$

where $\mathbf{Q}^{(\alpha)}$ is the skew-symmetric part of the Schmid tensor $\mathbf{T}^{(\alpha)}$. Rewriting Eq. (4) results in the crystal reorientation rate $\dot{\mathbf{R}}^*$, given by the difference between the crystal spin and the plastic spin due to slip,

$$\dot{\mathbf{R}}^* = \left(\mathbf{W}_c - \sum_\alpha \dot{\gamma}^{(\alpha)} \mathbf{Q}^{(\alpha)} \right) \mathbf{R}^*. \tag{5}$$

Eliminating $\dot{\gamma}^{(\alpha)}$ between Eqs. (1) and (3), and substituting Eq. (2) for $\tau^{(\alpha)}$ leads to an expression for the crystal deformation rate in terms of the deviatoric stress,

$$\mathbf{D}_c = \left[\sum_\alpha \frac{\dot{\gamma}_0}{\hat{\tau}} \left| \frac{\tau^{(\alpha)}}{\hat{\tau}} \right|^{(1/m)-1} \mathbf{P}^{(\alpha)} \otimes \mathbf{P}^{(\alpha)} \right] \boldsymbol{\sigma}'_c, \tag{6}$$

or

$$\mathbf{D}_c = \mathscr{S}_c \, \boldsymbol{\sigma}'_c, \tag{7}$$

where $\mathscr{S}_c$ is the crystal "compliance" tensor. The rate dependence of Eq. (1) permits inversion of Eq. (6), and expression of the crystal deviatoric stress under a given deformation rate as

$$\boldsymbol{\sigma}'_c = \mathscr{S}_c^{-1} \, \mathbf{D}_c. \tag{8}$$

The non-linear nature of the crystal constitutive Eq. (8) requires an iterative method to compute the deviatoric stress for a given rate of deformation. The anisotropic response due to the crystal orientation is reflected in the crystal compliance.

The plastic deformation of the material is modeled in incremental fashion, by solving the boundary value problem for material motion at each strain increment. Balance laws for equilibrium and mass conservation are applied in conjunction with the constitutive assumptions discussed above. Following the approach of Beaudoin et al. [9], a hybrid finite element formulation is employed for this purpose. Instead of developing the equilibrium statement from balance of momentum at the global level, here it is written as a balance of tractions at the inter-element boundaries. Weighted residuals are formed on the equilibrium statement and the constitutive relation. A third residual on the conservation of mass (which for the case of incompressible plastic deformation reduces to a divergence-free velocity field) completes the formulation. Interpolation functions are introduced for the nodal velocities, element stress components and the pressure. A proper choice of the shape functions for the stress permits elimination of the stress degrees of freedom at the element level. The result is a system of equations for the discretized velocity field, which is solved assuming fixed material state and geometry.

Upon obtaining a converged velocity solution, the material state and geometry are updated. The material is characterized by the orientation of the crystal and the hardness parameter. The reorientation rate given by Eq. (5) is used to update the orientation, while the hardness is evolved using a modified Voce type law [16–18],

$$\dot{\hat{\tau}} = H_0 \left(\frac{\hat{\tau}_s - \hat{\tau}}{\hat{\tau}_s - \hat{\tau}_i} \right) \dot{\gamma}^*, \tag{9}$$

where hardening rate H_0 and initial hardness $\hat{\tau}_i$ are material parameters. $\dot{\gamma}^*$ is a measure of the net shearing rate on all the slip systems,

$$\dot{\gamma}^* = \sum_\alpha |\dot{\gamma}^{(\alpha)}|. \tag{10}$$

The saturation hardness $\hat{\tau}_s$ based on the current slip system state is given by

$$\hat{\tau}_s = \hat{\tau}_{s_0}\left(\frac{\dot{\gamma}^*}{\dot{\gamma}_s}\right)^{m'}, \tag{11}$$

where $\hat{\tau}_{s_0}$, $\dot{\gamma}_s$ and m' are material parameters.

A few comments on the implementation of this formulation are in order. Development of the material response entails solution of the non-linear crystal constitutive relation for each element, and must be performed during each iteration for the velocity field at a given strain increment. In this respect, the methodology described above proves to be computationally demanding. Use of the hybrid approach leads to introduction of additional degrees of freedom for the crystal stresses, thereby adding to the computational burden associated with the stiffness calculations. The advantage of using this approach is the smoothness in the stress field, due to the enforcement of traction balance at the element interfaces in an approximate sense [9]. This proves particularly useful for situations where there are abrupt changes in material properties, as in the case of boundaries between grains. In the finite element context, the numerical integration required for computing the stiffness matrix can be performed concurrently for all elements. The choice of piecewise discontinuous interpolation functions for the stress is a key feature of the formulation, which enables computation of the stiffness matrices in concurrent fashion for all elements [9]. In turn, this feature enables exploitation of parallel computing technologies in order to greatly improve the feasibility of treating large three-dimensional discretizations.

While the stiffness computations are relatively straightforward to implement in a parallel environment, the solution of the resulting system of equations poses a greater challenge. Since direct solvers are difficult to optimize on a parallel machine, it is advantageous to use an iterative procedure, such as the conjugate gradient (CG) method [19]. In this context, enforcing the incompressibility constraint requires special attention, since it degrades the numerical condition of the resulting system of equations. In the current formulation, incompressibility is enforced using a modified consistent penalty approach, which seeks to decouple the solution for the pressure field from the CG method, as discussed by Beaudoin et al. [20]. A detailed discussion of the development of a parallel version of the formulation using High Performance Fortran (HPF) for the Intel PARAGON computer is available elsewhere [21].

2.1. Computation of stored energy and orientation data

The finite element simulations make use of the orientation information of the crystals in the form of Euler angles (ψ, θ, φ) using the convention of Kocks [22]. At the end of the deformation, the resulting Euler angles of the elements were transformed to axis-angle pairs for subsequent use in the Monte Carlo simulations of recovery and recrystallization [12]. The stored energy values were calculated based on the hardness parameters in each element. The evolution of the hardness parameter and orientation of each element based on the deformation rate in that element was computed using the equations discussed above.

It has been mentioned earlier that the hardness parameter $\hat{\tau}$ represents resistance to plastic deformation. It is hence taken to be proportional to the square root of the dislocation density [23],

$$\hat{\tau} = \tfrac{1}{2}Gb\rho^{1/2}, \tag{12}$$

where G is the shear modulus of the material and b is the magnitude of the Burgers vector. The stored energy (per unit volume) is given by the relation

$$H = \tfrac{1}{2}\rho G b^2. \tag{13}$$

Eqs. (12) and (13) can be combined to write the stored energy in terms of the hardness and the shear modulus as

$$H = \frac{2\hat{\tau}^2}{G}. \tag{14}$$

For the Monte Carlo simulations, it was advantageous to compute the natural invariants (axis-angle pair) of the orientation of each element. The invariants are the axis of rotation $\mathbf{c}$ and the angle of rotation ω about it. While Euler angles have been traditionally used for representing crystal orientations, the resulting space of orientations has certain undesirable properties [24]. Instead, the natural invariants can be combined to construct a class of "Neo-Eulerian" parameterizations to describe an orientation [24],

$$\mathbf{r} = f(\omega)\ \mathbf{c}, \tag{15}$$

by scaling the axis of rotation by a function of the angle. In particular, $f(\omega) = \tan(\omega/2)$ results in Rodrigues' parameters [24,25],

$$(r_x, r_y, r_z) = (c_x, c_y, c_z)\tan\frac{\omega}{2},$$

where (c_x, c_y, c_z) are the components of a unit vector corresponding to the axis of rotation $\mathbf{c}$. The choice of $f(\omega) = \sin(\omega/2)$ leads to the vector part of a quaternion, with $\cos(\omega/2)$ forming the fourth component,

$$(q_0, q_1, q_2, q_3) = \left(\cos\frac{\omega}{2}, c_x\ \sin\frac{\omega}{2}, c_y\ \sin\frac{\omega}{2}, c_z\ \sin\frac{\omega}{2}\right).$$

The components in Rodrigues' space are easily obtained from the quaternions by dividing the last three components by q_0.

The space of Rodrigues' parameters is unbounded for arbitrary orientations, but different points in the space can be the maps to symmetrically equivalent orientations. Considerations of symmetry under rotation permit the reduction of the space of interest to a fundamental sub-region, which is typically obtained by choosing the equivalent orientations nearest to the origin of the space. The task of computing the Rodrigues' parameters for an orientation given in terms of Euler angles is readily accomplished using quaternions [26]. However, this calculation does not always result in the quaternions in the fundamental sub-region. Under cubic crystal symmetry, there are 24 equivalent orientations [27,24]. In order to determine the equivalent set of quaternions lying in the fundamental sub-region, it is only necessary to compute $\cos(\omega/2)$ for all 24 quaternions, to check which one has the largest absolute value (for the smallest angle of rotation). The other three components can then be calculated only for that quaternion [25]. Further details on these calculations are given in Appendix A.

3. Application to simulate cold deformation

The finite element formulation discussed in the previous section has been used to simulate cold deformation corresponding to different strains under plane strain compression. The intent was to model the deformation conditions near the center of a sheet during cold rolling. Reductions in thickness of 50% and $66\frac{2}{3}$%, corresponding to compressive true strains of $\varepsilon = 0.7$ and $\varepsilon = 1.1$, respectively, were simulated using appropriate discretizations. In order to capture the inhomogeneous deformation of the grains, each grain was discretized with a fairly large number of eight-noded brick elements. Material properties based on mechanical test data for 1100 aluminum [16] were used for the simulation, and are listed in Table 1.

A Monte-Carlo grain growth algorithm [28] was used for obtaining the initial microstructure for the finite element calculations. A grid of $200 \times 200 \times 200$ points, each with a different starting orientation number, was used in the three-dimensional grain growth simulation. The simulation was run until a final average grain size of about 10 was obtained. The microstructures for use in the finite element simulations were obtained by taking suitable subsets of points from the large grid. For the case of $\varepsilon = 0.7$, a mesh of

Table 1
Material parameters for the polycrystal simulations

m	$\dot{\gamma}_0$	H_0	$\hat{\tau}_i$	τ_{s0}	$\dot{\gamma}_s$	m'
0.05	1.0 s^{-1}	58.41 MPa	27.17 MPa	61.80 MPa	5.0×10^{10} s^{-1}	0.005

$15 \times 30 \times 60$ elements was initialized with random orientations using a one-to-one correspondence between the elements and the grid points after grain growth. Grid points with the same number were part of the same grain, and thus elements corresponding to these points received the same initial orientation. In a similar fashion, the $\varepsilon = 1.1$ case was simulated using a finite element mesh of size $10 \times 30 \times 90$. The initial mesh in both cases was made up of elements which were cubes, so that the uniform spacing between them in each direction could be preserved as in the Monte-Carlo grid used for grain growth. The overall domain was a parallelepiped with sides in the same proportion as the number of elements in each direction, as illustrated in Fig. 1 for the case of $\varepsilon = 0.7$. Also shown in Fig. 1 is the microstructure indicating the discretization of each grain with a large number of elements. The colors used to depict the microstructure have no significance other than to distinguish the different grains.

Boundary conditions were applied to the mesh such that the material deformed by compression along the Z-axis and extension along the X-axis, with Y being the constrained direction. The normal velocities of nodes on the faces normal to $-X$ and $-Z$ were prescribed to be zero. On the opposite faces, the normal velocity components were prescribed such that a constant unit rate of deformation was maintained. When the element distortion became too severe, the mesh was reconstructed using regular elements with the proper aspect ratio based on the amount of strain. After deformation to the appropriate final strain, the aspect ratio of the overall mesh became 1:1:1, due to the choice of the initial mesh dimensions. The individual elements, which initially were cubes, elongated in the X-direction and reduced in length along the Z-direction. The aspect ratio of the elements on average in the X to Z-directions became the same as the ratio of elements in the Z to X-directions. Fig. 2 shows the deformed mesh and microstructure after a compressive strain of $\varepsilon = 0.7$. Examination of the deformed mesh clearly shows the non-uniform deformation of the microstructure. Individual elements undergo varying amounts of shear in addition to the extension along X and compression along Z.

After deformation to the appropriate strain, the hardness parameters for the elements were used to compute the stored energy of deformation using the procedure described in the Section 2.1. The stored energy distribution is hence a reflection of the hardening behavior of the microstructure. Shown in Fig. 3 are the initial and deformed microstructures, and the stored energy distribution, for a section of the microstructure taken normal to the constrained (Y) direction. It is seen that the stored energy has a non-uniform distribution both within a single grain and among the different grains. It is observed that the stored energy is higher close to some of the prior grain boundaries, as indicated in Fig. 3(c). However, it is important to note that not all grain boundaries develop high stored energy values. There are also regions within some of the bigger grains which show high stored energy, as in the grain at the bottom left corner. The stored energy enhancement at the grain boundaries compared to the grain interior depends on the local environment of the boundaries. If a grain is oriented favorably to accommodate the applied deformation, but is situated next to an unfavorably oriented grain, its boundary will be constrained by the second grain, leading to greater deformation in the interior.

The orientations of all elements which were part of the same grain were initialized with the same set of Euler angles. During deformation, the orientations of these elements evolved in accordance with the local velocity gradient. The final orientations were converted from Euler angles to axis-angle pairs, and Fig. 4 shows orientations before and after deformation in terms of the angles of the axis-angle pairs. Note that the initial angles have been depicted with the deformed mesh, to indicate the non-uniform reorientation of individual grains. The initial orientations of all elements in a grain are the same, so they all map to the same

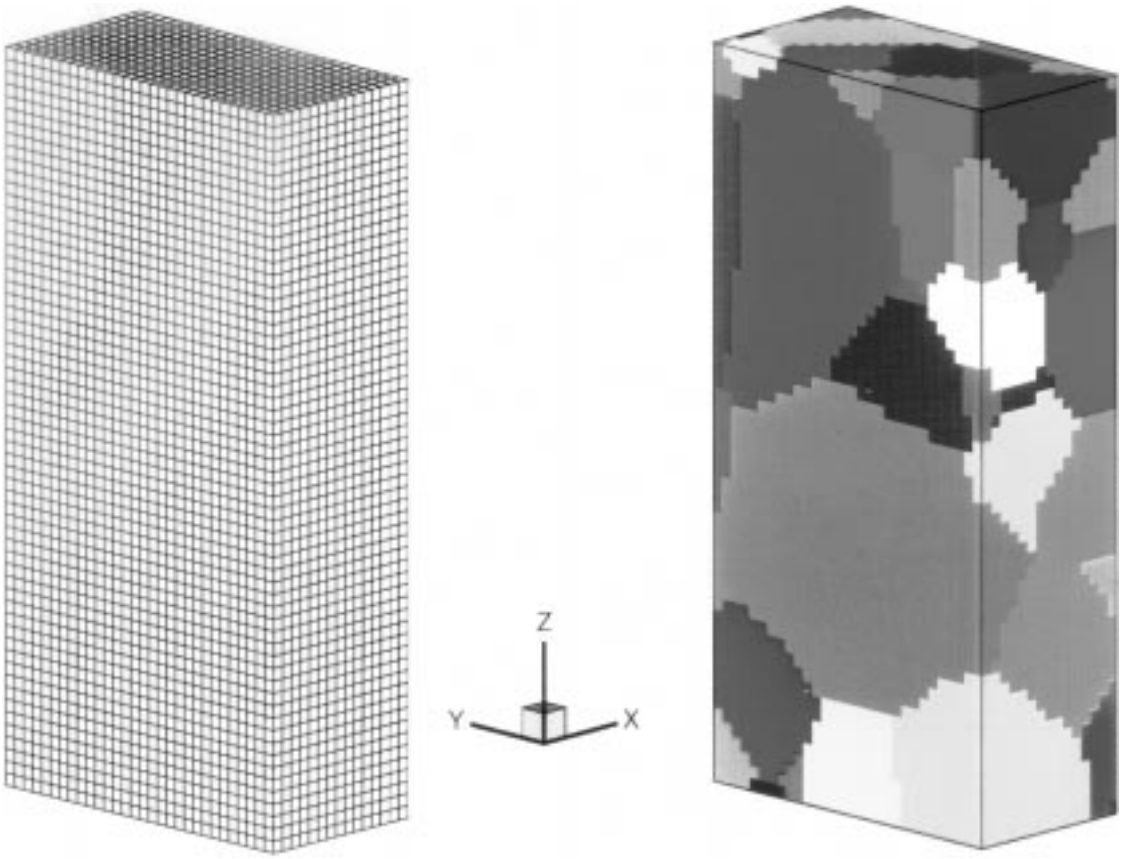

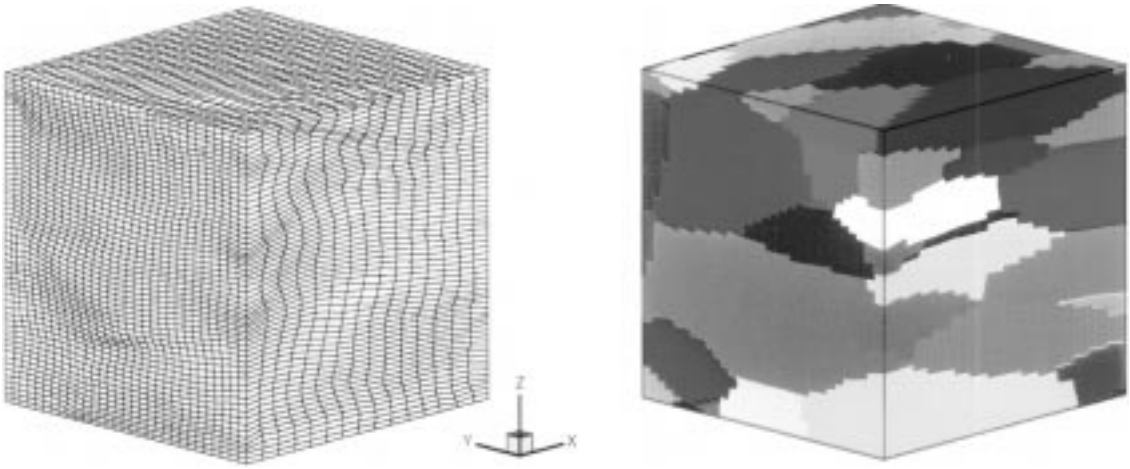

Fig. 1. Initial mesh of $15 \times 30 \times 60$ elements (left) and the microstructure (right) for the case of deformation to $\varepsilon = 0.7$.

Fig. 2. Mesh (left) and microstructure (right) after deformation to compressive strain of $\varepsilon = 0.7$.

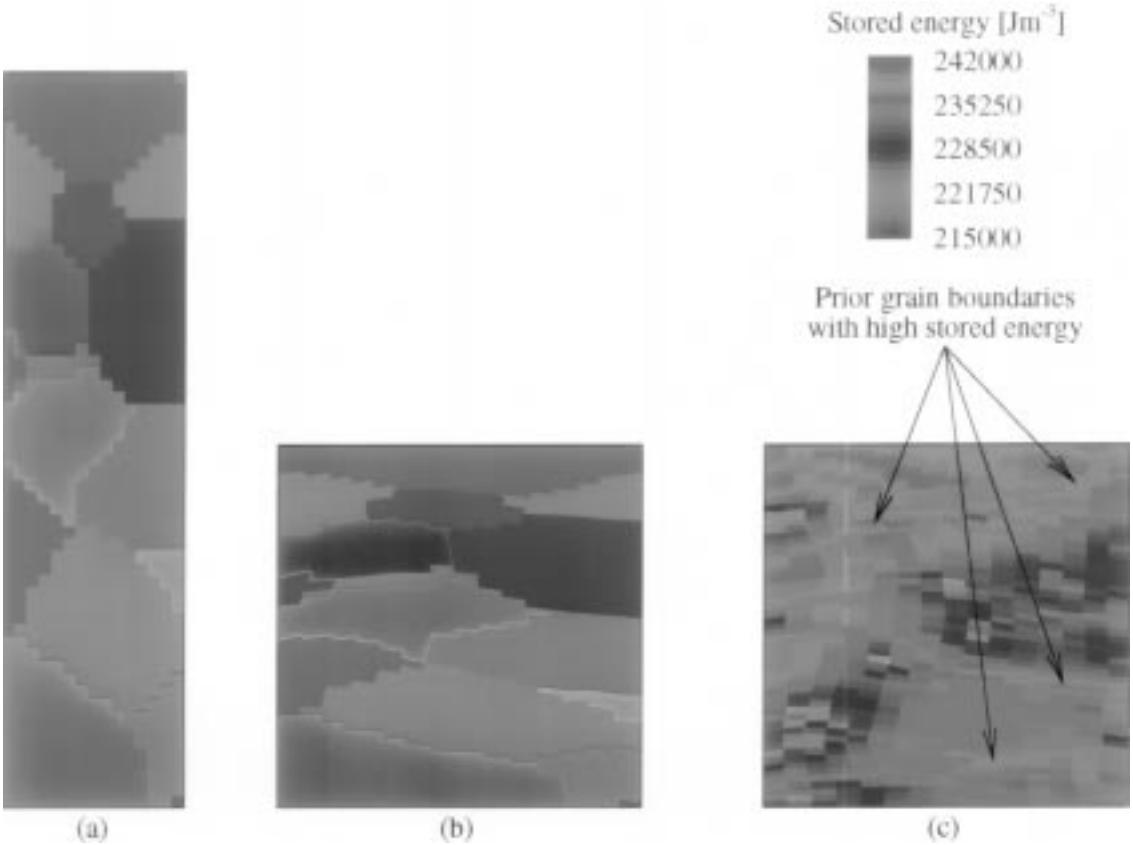

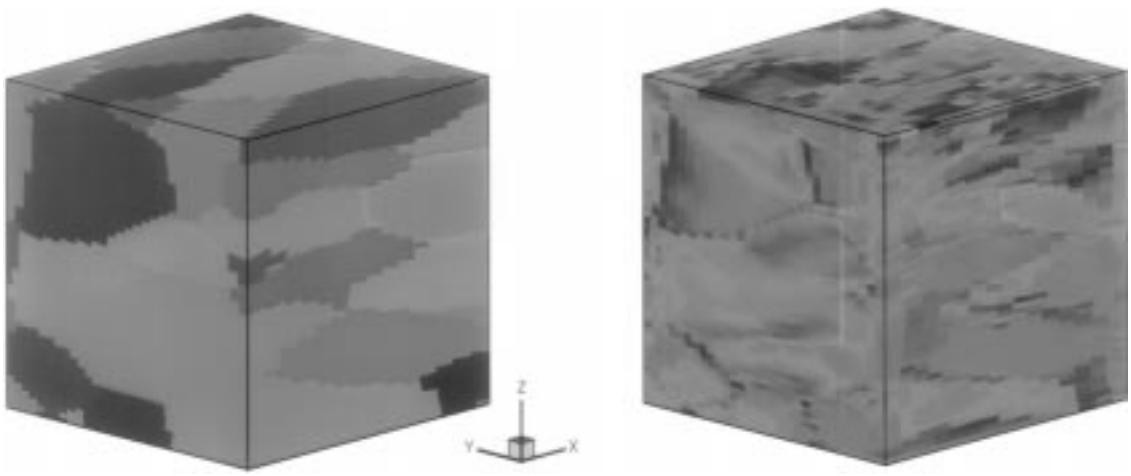

Fig. 3. (a) Initial microstructure, (b) deformed microstructure, and (c) stored energy distribution for a section taken normal to the constrained (Y) direction for deformation to $\varepsilon = 0.7$.

Fig. 4. Map of the angles from the axis-angle representation for the initial (left) and final (right) orientations for the case of deformation to $\varepsilon = 0.7$.

color. After deformation to the appropriate strain, elements which are part of the same grain show different angles, indicating breakup of the grains. It must be mentioned here that the axis of rotation has not been included in the plot, and hence the orientation information is incomplete. Nevertheless, it clearly indicates the capability of the simulation method to capture the non-uniform orientation distribution.

The distribution of orientations is shown in Fig. 5 for a section taken normal to the constrained (Y) direction. The original microstructure shows the grains before deformation, and the deformed microstructure shows the angles from the axis-angle representations of the initial and final orientations. Since there is clearly a non-uniform pattern in the reorientation of the grains, a plot of the average misorientation of each element with its neighbors was constructed, as shown in Fig. 6. For computing the average misorientation, first the misorientation of the element in question with each first nearest neighbor was determined using the procedure described in Appendix A. The average of all the angles (ignoring the axes) considering only the elements which were part of the same grain according to the original microstructure was then computed to obtain the average misorientation. Thus, the result of this calculation using the starting orientations would lead to zero misorientation for all the elements. The intent was to avoid neighboring elements if they were part of a different grain, so that the misorientation would be a measure of deviations in reorientation in the same grain. As seen from Fig. 6, there are some bands of elements with a high average misorientation with first nearest neighbors. While most of the bands correlate well with prior grain boundaries, some of these bands pass right through the middle of a grain, indicating different deformation paths for elements on either side. An instance of such a band is indicated by the elements

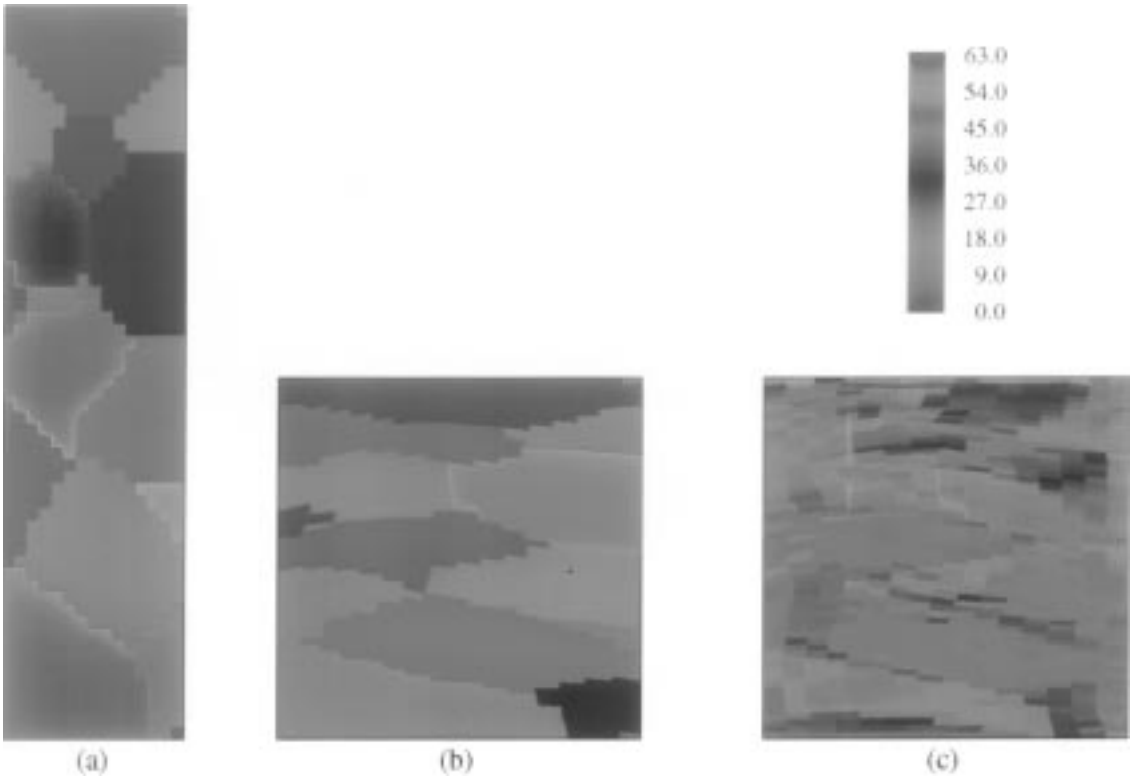

Fig. 5. (a) Initial microstructure, (b) angles from initial orientations mapped to the deformed microstructure, and (c) angles from final orientations for a section taken normal to the constrained (Y) direction after strain of $\varepsilon = 0.7$.

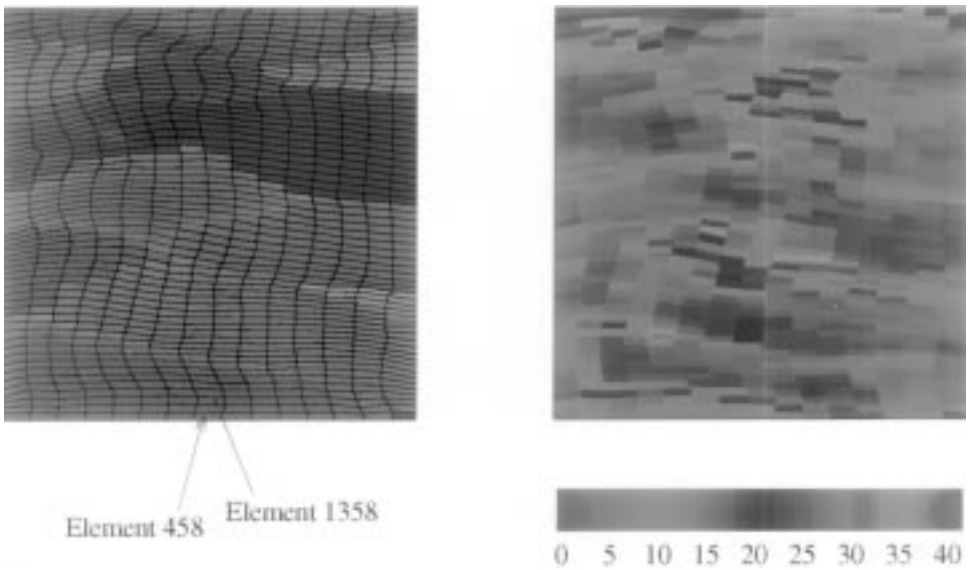

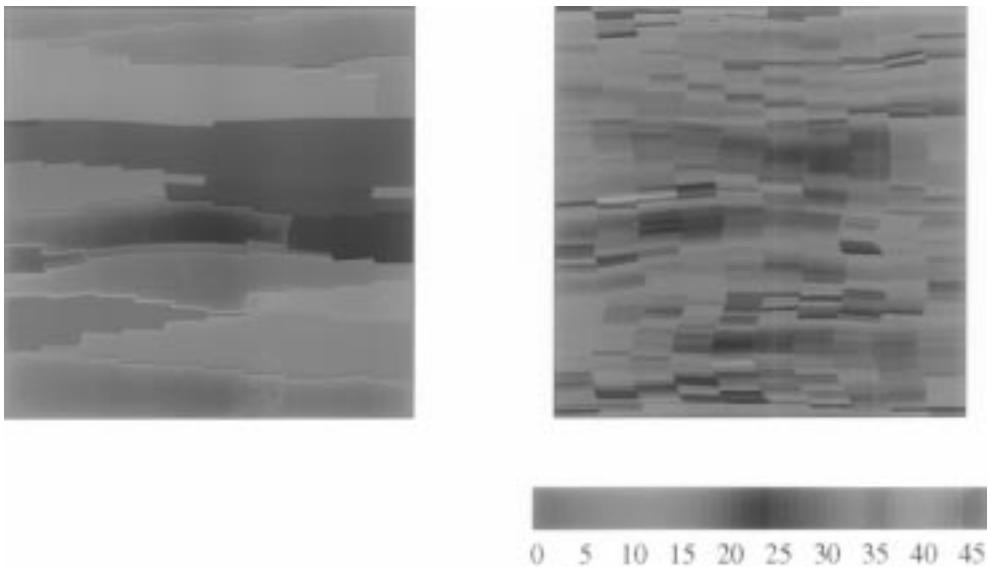

Fig. 6. Deformed microstructure showing the mesh (left) and the average misorientation of the elements with nearest neighbors (right) for a section taken normal to the constrained (Y) direction after strain of $\varepsilon = 0.7$.

Fig. 7. Deformed microstructure (left) and the average misorientation of the elements with nearest neighbors (right) for a section taken normal to the constrained (Y) direction after strain of $\varepsilon = 1.1$.

numbered 458 and 1358 on either side of the band. It is seen from Fig. 6 that the shearing of these adjacent elements is in opposite directions, and leads to high misorientation values. Fig. 7 shows the deformed microstructure and the average misorientation for a section taken in the X-Z plane for the case of $\varepsilon = 1.1$.

Once again, there are high misorientation regions near grain boundaries as well as in the interior of some large grains.

The distribution of average misorientations computed for all the elements is shown in Fig. 8 in the form of histograms. For the case of 50% reduction, the majority of misorientations are rather small, and the drop is fairly steep, with maximum values around 25°. At the higher deformation level, the spread is wider with less number of elements having low misorientations, and the maximum misorientation angle is about 35°. These results correlate quite well with the experimental data reported by Juul Jensen [29]. Even though the measurements are carried out at a much smaller length scale than the simulations, the qualitative and quantitative match between the two is quite remarkable.

3.1. Texture evolution

The Euler angles used to initialize the orientations of the elements for the polycrystal simulations were obtained by a random sampling of Euler space. Fig. 9 shows the pole figures from the initial orientations used for the deformation to $\varepsilon = 0.7$ in the form of a point plot. The same set of orientations is also shown in Fig. 10, but now the orientations are weighted by the number of elements used to discretize a grain at that orientation in the finite element mesh, leading to a non-random texture. The orientations were processed using the DIOR program from popLA [30] with cubic crystal symmetry, followed by a Gaussian smoothing operation, to generate the pole figures shown in equal area projection. The initial texture for the orien-

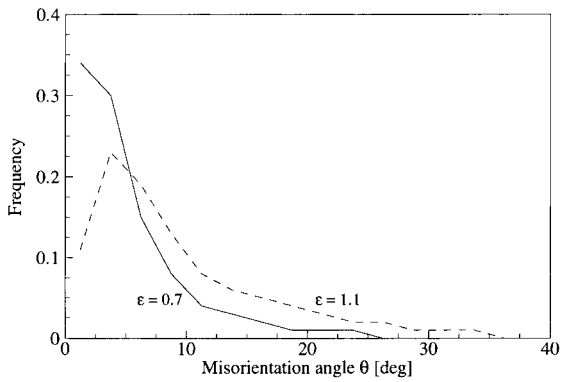

Fig. 8. Histograms showing the distributions of average misorientations for deformation to $\varepsilon = 0.7$ and 1.1.

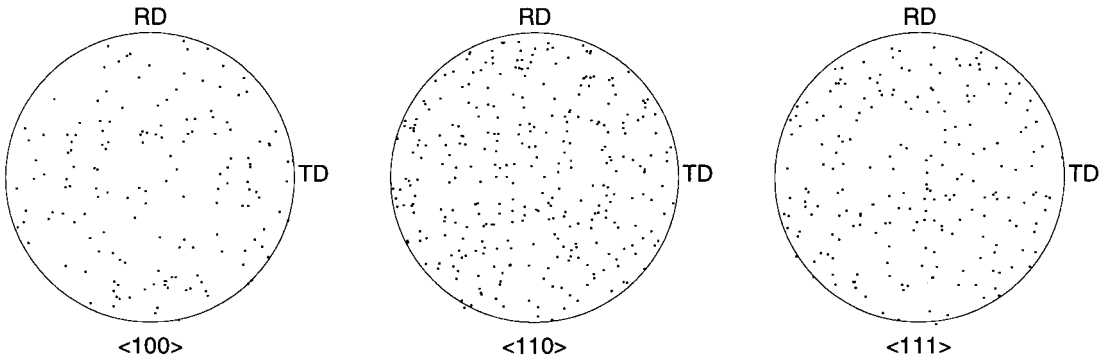

Fig. 9. Pole figures showing the initial orientations used for the case of deformation to $\varepsilon = 0.7$.

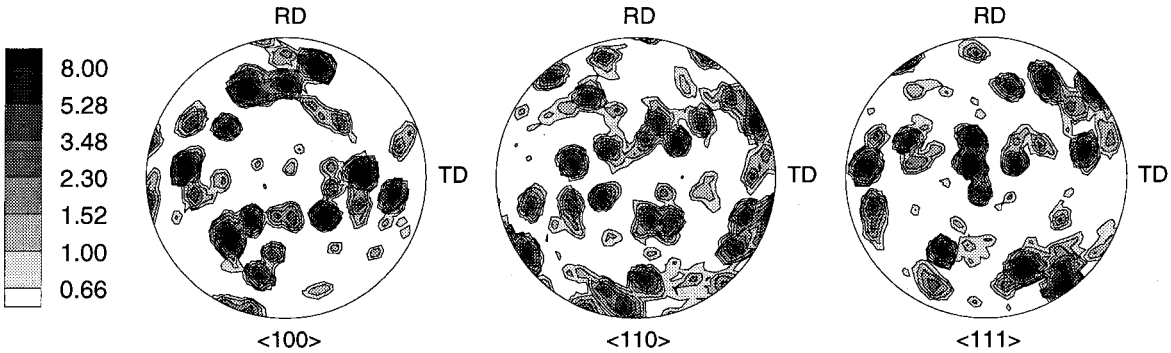

Fig. 10. Pole figures in equal area projection representing the initial texture used for the case of deformation to $\varepsilon = 0.7$. Contour levels represent multiples of random texture intensity on a logarithmic scale.

tations used in the $\varepsilon = 1.1$ case are shown in Fig. 11. Note that the choice of the mesh sizes leads to different microstructures for the two cases, and hence different initial textures.

After deformation to compressive strains of $\varepsilon = 0.7$ and 1.1, respectively, each element had a different orientation. Since there were 27,000 elements in the mesh for each case, the resulting orientations were again processed using the DIOR program, with the application of cubic crystal symmetry and orthotropic sample symmetry. The textures after the two strains are shown in Figs. 12 and 13, respectively. Deformation by plane strain compression leads to development of texture components typically observed after cold rolling [31,32], such as $\{1\,1\,2\}\langle 1\,1\,1\rangle$ copper, $\{1\,2\,3\}\langle 6\,3\,4\rangle$ S and $\{0\,1\,1\}\langle 2\,1\,1\rangle$ brass orientations (shown in Fig. 14). However, the initial texture plays a significant role in the relative intensities of these components. The texture for deformation to $\varepsilon = 0.7$ shows a strong $\{1\,2\,3\}\langle 6\,3\,4\rangle$ S component and a weaker $\{1\,1\,2\}\langle 1\,1\,1\rangle$ copper component, whereas the opposite is true for the texture after deformation to $\varepsilon = 1.1$. The different final textures are a result of the different initial microstructures, indicating the influence of the starting orientations.

The development of deformation bands in the grains due to the inhomogeneous straining has been discussed earlier. Fig. 15 shows the evolution of the orientations of two adjacent elements which started with identical orientations, but evolved in different directions. These two elements are marked by their

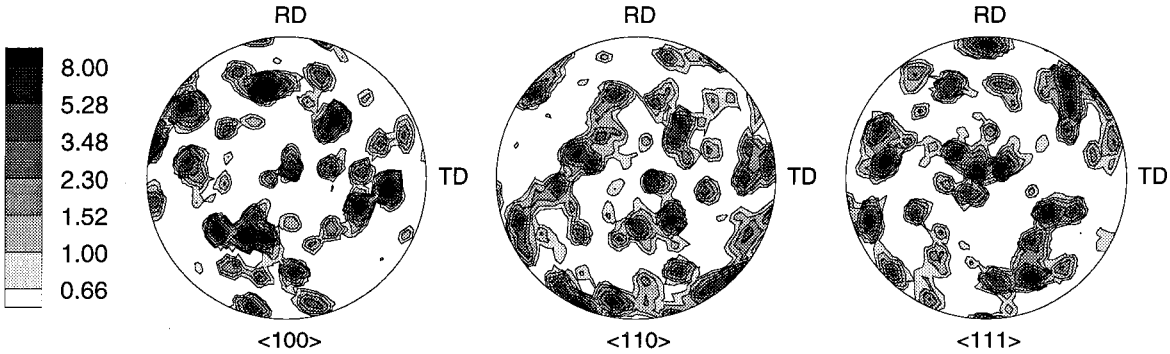

Fig. 11. Pole figures in equal area projection representing the initial texture used for the case of deformation to $\varepsilon = 1.1$. Contour levels represent multiples of random texture intensity on a logarithmic scale.

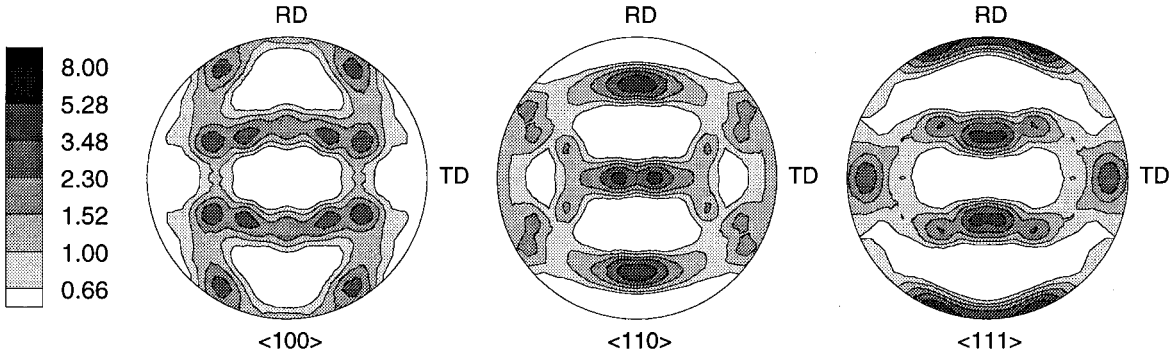

Fig. 12. Pole figures in equal area projection showing the texture after deformation to $\varepsilon = 0.7$. Contour levels represent multiples of random texture intensity on a logarithmic scale.

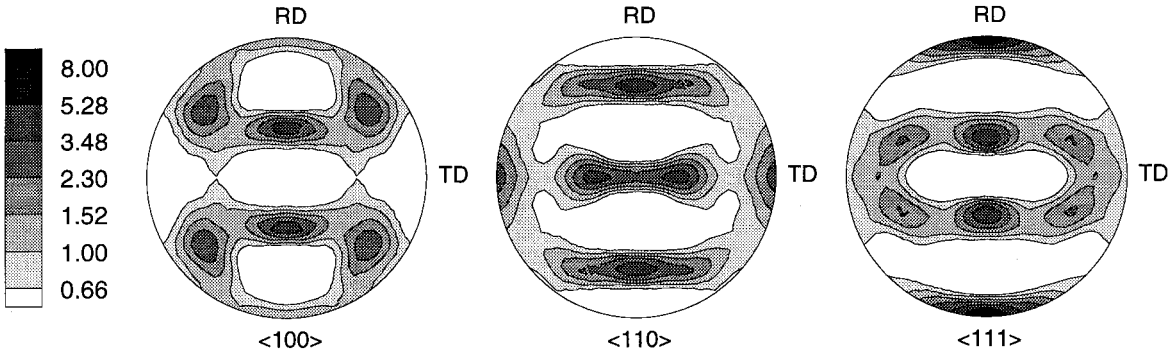

Fig. 13. Pole figures in equal area projection showing the texture after deformation to $\varepsilon = 1.1$. Contour levels represent multiples of random texture intensity on a logarithmic scale.

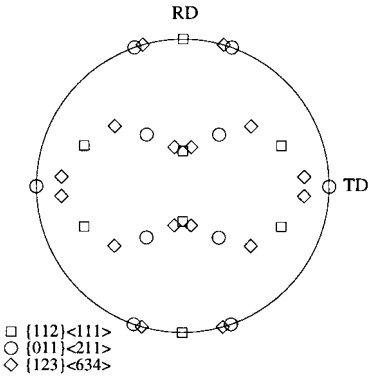

Fig. 14. ⟨1 1 1⟩ pole figure in equal area projection showing some ideal orientations commonly found in rolling textures.

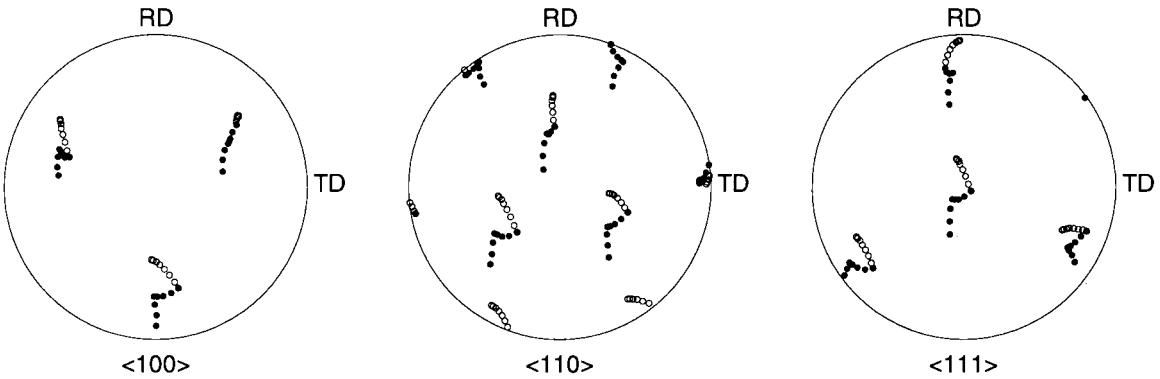

Fig. 15. Evolution of orientations of two adjacent elements in the same grain shown as pole figures in equal area projection. The elements are marked in Fig. 6 as 458 (shown here with •) and 1358 (shown here with ○).

numbers in Fig. 6, and are seen to undergo shear deformation in opposite directions. The orientations of these two elements are indicated in the pole figures in Fig. 15 at strain increments of every 10% in the form of filled (element 458) and open circles (element 1358), showing the reorientation in different directions. These orientation gradients play a significant role in the nucleation of strain-free grains during subsequent annealing [12].

4. Conclusions

The deformation of polycrystals has been simulated by making use of the finite element method. By means of discretization at the level of individual grains, it was possible to monitor the non-uniform deformations of the grains. A constitutive model based on crystal plasticity was used to track the orientation and hardness values of the elements. The anisotropic material response due to the limited deformation modes available through crystallographic slip was included in the formulation through this approach.

Two different meshes were constructed to simulate deformation in plane strain compression of a material with FCC crystal structure to different final strains. The results demonstrate the capability of the formulation to capture the inhomogeneous deformation of grains during the plastic deformation of polycrystals. The stored energy of deformation related to increased dislocation density was computed from the hardness of the elements, and the orientation data were transformed to an axis-angle representation. It was observed that the enhancement of the stored energy at the boundaries relative to the interior of a grain depends on the local orientations of the neighboring grains, which dictate how much deformation is accommodated by the boundary regions. While some boundaries show higher stored energy values, others show lower values than interior regions. It is known that such regions are the possible sites for nucleation of recrystallized grains. In a similar fashion, the orientations of the elements showed non-uniform distributions, with elements which received the same initial orientations as part of the same grain evolving to different final orientations. There was clearly an effect of the neighboring grains on the deformation of each grain, with the resulting constraints leading to different degrees of inhomogeneity.

It must be noted here that development of the finite element formulation for massively parallel computers is a key feature which enabled the use of large three-dimensional discretizations. In studying the deformation of polycrystals, it is necessary to choose a representative sample consisting of a reasonable number of grains. Capturing the gradients within individual grains requires placing a large number of elements in each grain. This leads to a refined discretization with thousands of elements. If one now adds

the complexity of the constitutive response due to the nature of the crystal plasticity model, and the degradation in the condition of the system due to the incompressibility constraint, the computational expense is so large that it is only feasible on a parallel architecture.

The strength of the simulation technique lies in its ability to provide quantitative information on the distributions of stored energy and orientations among the elements. The data from these simulations have been used for modeling the process of static recrystallization using the Monte Carlo method [12]. By providing quantitative information on the orientation and stored energy distributions in the cold worked microstructure, the current simulations have enabled the modeling of nucleation phenomena during recrystallization, in turn leading to the prediciton of recrystallization textures. Such detailed simulations at the microstructural length scales provide information on the deformation of polycrystals which can then be used for developing better models for use in simulations of bulk deformation at the continuum scales.

Acknowledgements

This research was sponsored by the Division of Materials Science, US Department of Energy, under contract DE-AC05-96OR22464 with Lockheed Martin Energy Research Corporation. The research was supported in part by an appointment to the Oak Ridge National Laboratory Postdoctoral Research Associates Program administered jointly by the Oak Ridge National Laboratory and the Oak Ridge Institute for Science and Education. The authors acknowledge the use of the Intel PARAGON XP/S 35 located in the Oak Ridge National Laboratory Center for Computational Sciences (CCS), funded by the Department of Energy's Office of Scientific Computing.

Appendix A. Computation of natural invariants

Given the Euler angles (ψ, θ, φ) to describe the orientation of a crystal [22], it is of interest to compute the natural invariants, i.e., an axis-angle pair, to represent the orientation. For this purpose, it is convenient to first convert the angles to a rotation matrix. While this is not a necessary step for a single orientation, it is useful for computing the misorientation between two crystals. The rotation matrix is given by

$$[R] = \begin{bmatrix} -\sin\psi\sin\varphi - \cos\psi\cos\theta\cos\varphi & \sin\psi\cos\varphi - \cos\psi\cos\theta\sin\varphi & \cos\psi\sin\theta \\ \cos\psi\sin\varphi - \sin\psi\cos\theta\cos\varphi & -\cos\psi\cos\varphi - \sin\psi\cos\theta\sin\varphi & \sin\psi\sin\theta \\ \sin\theta\cos\varphi & \sin\theta\sin\varphi & \cos\theta \end{bmatrix}.$$

The angle of rotation ω, and the components of a unit vector corresponding to the axis of rotation $\mathbf{c}$, are then obtained as [25,27]

$$\omega = \arccos\left[\tfrac{1}{2}(\mathrm{Tr}(R) - 1)\right],$$
$$c_x = \frac{R_{32} - R_{23}}{2\sin\omega},$$
$$c_y = \frac{R_{13} - R_{31}}{2\sin\omega},$$
$$c_z = \frac{R_{21} - R_{12}}{2\sin\omega}.$$

In computing the angle and axis using the above expressions, care must be taken for angles close to the limits of 0° or 180° to avoid numerical difficulties.

For the case of crystals with symmetries under rotation, it is possible for different orientations to be symmetrically equivalent, e.g., a rotation of 90° about the $\langle 1\,0\,0\rangle$ axes for a cubic crystal. Under such

conditions, the three-dimensional space of orientations can be reduced to a fundamental sub-region, within which all possible orientations can be found. While there are clearly an infinite number of choices for such a sub-region, it is common to consider a sub-region obtained by choosing the equivalent orientation which gives the smallest angle of rotation. In this sub-region, each point represents a unique orientation. For any point outside the sub-region, an equivalent orientation which lies inside the sub-region can be found by a symmetry operation.

For cubic crystals, there are 24 symmetrically equivalent orientations [27,24]. The task of finding the orientation with the smallest angle is accomplished by making use of quaternions. The quaternions for the axis-angle pair $(\mathbf{c}, \omega)$ are given by [27]

$$(q_0, q_1, q_2, q_3) = \left(\cos\frac{\omega}{2}, c_x \sin\frac{\omega}{2}, c_y \sin\frac{\omega}{2}, c_z \sin\frac{\omega}{2}\right).$$

It is clear that the smallest angle corresponds to the largest q_0. Hence, finding the quaternion which lies in the fundamental region requires computing the value of q_0 for all 24 quaternions, and choosing the one which has the largest absolute value. Calculation of the value of q_0 for the symmetrically equivalent quaternions under cubic symmetry is performed using

$$q_0' = q_0 s_0 - q_1 s_1 - q_2 s_2 - q_3 s_3,$$

where the values of (s_0, s_1, s_2, s_3) are listed in Table 2 for cubic symmetry [27].

Once the quaternion with the maximum q_0' is determined, then the other components for that equivalent set of quaternions are computed using the rules of quaternion algebra [26,25] as

Table 2
Quaternions which are equivalent under cubic symmetry

	s_0	s_1	s_2	s_3
1	1	0	0	0
2	0	1	0	0
3	0	0	1	0
4	0	0	0	1
5	$1/\sqrt{2}$	$1/\sqrt{2}$	0	0
6	$1/\sqrt{2}$	0	$1/\sqrt{2}$	0
7	$1/\sqrt{2}$	0	0	$1/\sqrt{2}$
8	$1/\sqrt{2}$	$-1/\sqrt{2}$	0	0
9	$1/\sqrt{2}$	0	$-1/\sqrt{2}$	0
10	$1/\sqrt{2}$	0	0	$-1/\sqrt{2}$
11	0	$1/\sqrt{2}$	$1/\sqrt{2}$	0
12	0	$1/\sqrt{2}$	0	$1/\sqrt{2}$
13	0	0	$1/\sqrt{2}$	$1/\sqrt{2}$
14	0	$1/\sqrt{2}$	$-1/\sqrt{2}$	0
15	0	$1/\sqrt{2}$	0	$-1/\sqrt{2}$
16	0	0	$1/\sqrt{2}$	$-1/\sqrt{2}$
17	1/2	1/2	1/2	1/2
18	1/2	1/2	1/2	−1/2
19	1/2	1/2	−1/2	1/2
20	1/2	−1/2	1/2	1/2
21	1/2	1/2	−1/2	−1/2
22	1/2	−1/2	1/2	−1/2
23	1/2	−1/2	−1/2	1/2
24	1/2	−1/2	−1/2	−1/2

$$q_0' = q_0 s_0 - q_1 s_1 - q_2 s_2 - q_3 s_3,$$
$$q_1' = q_0 s_1 + q_1 s_0 + q_2 s_3 - q_3 s_2,$$
$$q_2' = q_0 s_2 - q_1 s_3 + q_2 s_0 + q_3 s_1,$$
$$q_3' = q_0 s_3 + q_1 s_2 - q_2 s_1 + q_3 s_0.$$

Having determined the quaternions corresponding to the smallest angle, the axis and angle can then be computed using

$$\omega = 2 \arccos(q_0'),$$
$$c_x = q_1' \Big/ \sin\frac{\omega}{2},$$
$$c_y = q_2' \Big/ \sin\frac{\omega}{2},$$
$$c_z = q_3' \Big/ \sin\frac{\omega}{2}$$

Computing the misorientation between two crystals with different orientations can follow the procedure outlined above, once the matrix corresponding to the rotation from orientation 1 to 2 is determined,

$$[R] = [R_2][R_1]^{\mathrm{T}},$$

where the subscripts refer to the two orientations. The axis and angle pair describing the misorientation between the two crystals is then determined.

References

[1] D. Hull, D.J. Bacon, Introduction to Dislocations, Pergamon Press, Oxford, 1984.
[2] S.V. Harren, R.J. Asaro, J. Mech. Phys. Solids 37 (1989) 191.
[3] R. Becker, J.F. Butler Jr, H. Hu, L.A. Lalli, Metall. Trans. 22A (1991) 45.
[4] R. Becker, Acta Metall. 39 (1991) 1211.
[5] C.A. Bronkhorst, S.R. Kalidindi, L. Anand, Philos. Trans. Roy. Soc. London Ser. A 341 (1992) 443.
[6] L. Anand, S.R. Kalidindi, Mech. Mater. 17 (1994) 223.
[7] R. Becker, S. Panchanadeeswaran, Acta Mater. 43 (1995) 2701.
[8] G.I. Taylor, J. Inst. Metals 62 (1938) 307.
[9] A.J. Beaudoin, P.R. Dawson, K.K. Mathur, U.F. Kocks, Int. J. Plasticity 11 (1995) 501.
[10] G.B. Sarma, P.R. Dawson, Acta Mater. 44 (1996) 1937.
[11] A.J. Beaudoin, H. Mecking, U.F. Kocks, Philos. Mag. A73 (1996) 1503.
[12] B. Radhakrishnan, G.B. Sarma, T. Zacharia, Acta Mater 46 (1998) 4415.
[13] J.W. Hutchinson, Proc. Roy. Soc. London Ser. A 348 (1976) 101.
[14] J. Pan, J.R. Rice, Int. J. Solids Struct. 19 (1983) 973.
[15] R.J. Asaro, A. Needleman, Acta Metall. 33 (1985) 923.
[16] K.K. Mathur, P.R. Dawson, Int. J. Plasticity 5 (1989) 67.
[17] E. Voce, Acta Metall. 51 (1948) 219.
[18] U.F. Kocks, J. Eng. Mater. Tech. 98 (1976) 76.
[19] R. Barrett, M. Berry, T. Chan, J. Demmel, J. Donato, J. Dongarra, V. Eijkhout, R. Pozo, C. Romine, H. van der Vorst, Templates for the Solution of Linear Systems: Building Blocks for Iterative Methods, SIAM, Philadelphia, 1994.
[20] A. J Beaudoin, P.R. Dawson, K.K. Mathur, U.F. Kocks, D.A. Korzekwa, Comput. Methods Appl. Mech. Engrg. 117 (1994) 49.
[21] G. Sarma, T. Zacharia, D. Miles, Comp. and Math. with Applic. 35 (1998) 41.
[22] U.F. Kocks, in: J.S. Kallend, G. Gottstein (Eds.), Proceedings of the Eighth International Conference on the Textures of Materials (ICOTOM 8), TMS Warrendale, 1988, p. 31.
[23] F.J. Humphreys, M. Hatherly, Recrystallization and Related Annealing Phenomena, Elsevier, Oxford, 1995.
[24] F.C. Frank, in: J.S. Kallend, G. Gottstein (Eds.), Proceedings of the Eighth International Conference on the Textures of Materials (ICOTOM 8), TMS Warrendale, 1988, p. 3.

[25] R. Becker, S. Panchanadeeswaran, Textures Microstruct. 10 (1989) 167.
[26] S.L. Altman, Rotations, Quaternions, and Double Groups, Clarendon Press, Oxford, 1986.
[27] H. Grimmer, Acta Crystallogr. A30 (1974) 685.
[28] B. Radhakrishnan, T. Zacharia, Metall. Mater. Trans. A 26 (1995) 167.
[29] D. Juul Jensen, Mater. Sci. Eng. A 234/236 (1997) 762.
[30] J.S. Kallend, U.F. Kocks, A.D. Rollett, H.-R. Wenk, Mater. Sci. Engrg. A 132 (1991) 1.
[31] J. Hirsch, K. Lücke, Acta Metall. 36 (1988) 2883.
[32] G.B. Sarma, P.R. Dawson, Int. J. Plasticity 12 (1996) 1023.